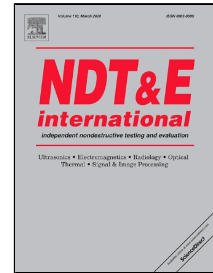


Multi-Scale Gapped Smoothing Algorithm for Robust Baseline-free Damage Detection in Optical Infrared Thermography

Gaétan Poelman, Saeid Hedayatrasa, Joost Segers, Wim Van Paepegem, Mathias Kersemans



PII: S0963-8695(19)30548-1
DOI: <https://doi.org/10.1016/j.ndteint.2020.102247>
Reference: JNDT 102247

To appear in: *NDT and E International*

Received Date: 06 September 2019
Accepted Date: 02 March 2020

Please cite this article as: Gaétan Poelman, Saeid Hedayatrasa, Joost Segers, Wim Van Paepegem, Mathias Kersemans, Multi-Scale Gapped Smoothing Algorithm for Robust Baseline-free Damage Detection in Optical Infrared Thermography, *NDT and E International* (2020), <https://doi.org/10.1016/j.ndteint.2020.102247>

This is a PDF file of an article that has undergone enhancements after acceptance, such as the addition of a cover page and metadata, and formatting for readability, but it is not yet the definitive version of record. This version will undergo additional copyediting, typesetting and review before it is published in its final form, but we are providing this version to give early visibility of the article. Please note that, during the production process, errors may be discovered which could affect the content, and all legal disclaimers that apply to the journal pertain.

Multi-Scale Gapped Smoothing Algorithm for Robust Baseline-free Damage Detection in Optical Infrared Thermography

Gaétan Poelman^{1,2,*}, Saeid Hedayatrasa^{1,2}, Joost Segers¹, Wim Van Paepegem¹
and Mathias Kersemans¹

¹ Mechanics of Materials and Structures (UGent-MMS), Department of Materials, Textiles and Chemical Engineering, Ghent University, Technologiepark-Zwijnaarde 46, 9052 Zwijnaarde, Belgium

² SIM Program M3 DETECT-IV, Technologiepark-Zwijnaarde 48, B-9052 Zwijnaarde, Belgium

* Corresponding author: Gaetan.Poelman@UGent.be

Abstract

Flash thermography is a promising technique to perform rapid non-destructive testing of composite materials. However, it is well known that several difficulties are inherently paired with this approach, such as non-uniform heating, measurement noise and lateral heat diffusion effects. Hence, advanced signal-processing techniques are indispensable in order to analyze the recorded dataset. One such processing technique is Gapped Smoothing Algorithm, which predicts a gapped pixel's value in its sound state from a measurement in the defected state by evaluating only its neighboring pixels. However, the standard Gapped Smoothing Algorithm uses a fixed spatial gap size, which induces issues to detect variable defect sizes in a noisy dataset.

In this paper, a Multi-Scale Gapped Smoothing Algorithm (MSGSA) is introduced as a baseline-free image processing technique and an extension to the standard Gapped Smoothing Algorithm. The MSGSA makes use of the evaluation of a wide range of spatial gap sizes so that defects of highly different dimensions are identified. Moreover, it is shown that a weighted combination of all assessed spatial gap sizes significantly improves the detectability of defects and results in an (almost) zero-reference background. The technique thus effectively suppresses the measurement noise and excitation non-uniformity. The efficiency of the MSGSA technique is evaluated and confirmed through numerical simulation and an experimental procedure of flash thermography on carbon fiber reinforced polymers with various defect sizes.

Keywords: Multi-scale Gapped Smoothing Algorithm (MSGSA), Non-destructive testing (NDT), Flash thermography, Image processing, Composites, CFRP

1. Introduction

Fiber reinforced polymers (FRPs) are composite materials that exhibit multiple advantageous properties such as a high specific stiffness/strength and a good corrosion resistance. This makes these materials interesting for a specific range of industries, e.g. aerospace and automotive. However, due to their layered structure, composites are prone to internal damage features which may arise either during manufacturing or during in-service loading, and which could ultimately lead to catastrophic failure of the component or the entire structure. Thus, in order to guarantee a composite component's structural integrity, proper non-destructive inspection techniques are indispensable.

Optical infrared thermography (IRT) is a fairly recent and promising non-destructive testing (NDT) technique in which the contrast in thermal properties between the sound material and a defect is exploited [1]. An optical source is used to thermally stimulate the sample's surface, while at the same time, a high-sensitivity infrared (IR) camera records the emitted infrared radiation from

the surface. The induced thermal gradient through the material's thickness causes thermal waves to diffuse into the specimen, where they interact with internal anomalies due to a thermal diffusivity mismatch. This interaction results in a local heat gradient at the recorded surface, making it possible to trace hidden anomalies. Optical IRT is inherently limited due to the diffusive and strongly damped nature of the excited thermal waves, making the inspection of highly anisotropic materials and the detection of deep and small defects very challenging.

Nowadays, several optical IRT implementations, classified based on the implemented excitation signal, are topics of investigation. In lock-in thermography (LT), halogen lamps are employed to excite the sample with a single-frequency sinusoidal signal [2-4], while in phase-locked restored pseudo heat flux thermography the halogen lamps excite with a periodic square wave [5]. Thermal wave radar (TWR) on the other hand exploits the use of advanced frequency and/or phase modulated waveforms for better defect detectability and depth probing [6-9]. Step-heating thermography (SHT) [10] and the recently proposed long-pulse thermography (LPT) [11, 12] both apply step-pulse heating for a specific period of time (e.g. 5-10 s). Recently, dynamic scanning thermography, in which both the excitation and the IR camera are translated over the sample, has also been applied successfully for the rapid detection of hidden defects [13]. For flash thermography (FT), a flash tube is used to provide an intense stimulation of only a few milliseconds to rapidly heat up the sample's surface [3, 14, 15].

Apart from the advanced excitation strategies listed above, advanced post-processing techniques have been developed with the goal to reduce noise and enhance defect detectability. Especially for flash thermography, adequate post-processing is indispensable to improve defect detectability. The most commonly used and well-known data analysis approaches for flash thermography are pulsed phase thermography (PPT) [16, 17], principal component thermography (PCT) [18], thermographic signal reconstruction (TSR) [19] and dynamic thermal tomography (DTT) [20, 21]. A more exhaustive list of processing techniques can be found in [22]. Besides data processing techniques, which exploit all available information in the recorded sequence, image processing techniques aim at enhancing the defect detectability by only considering one specific frame in time. For example, the median filtering passes a smoothing kernel so that spiky features are filtered from the image, while a Sobel filter may be applied for improved edge extraction [23]. Recently, gapped smoothing algorithm (GSA) was applied to flash thermographic data as a baseline-free image processing technique, showing promising results by obtaining an almost zero reference background [24].

The origin of the GSA approach is found in vibrational testing where it was introduced as a 1D processing technique applied on a beam structure [25]. The vibrational behavior of a beam in its sound state is estimated from a measurement in its damaged state, making this approach baseline-free. The underlying basis of the technique is to estimate a sound value for any individual cell of the measurement grid by a cubic interpolation of its surrounding cells. Since the original value of the cell itself (i.e. the spatial gap) is excluded from the interpolation, it is less likely that the interpolated value is affected by local anomalies, and therefore it is a good representative of the response of a sound material. Next, a damage index is defined as the squared difference between the measurement and the estimated sound state. Through this approach, localized thickness changes as small as 0.5% in a beam were successfully detected, where other vibrational approaches only managed to retrieve much more severe damages [25, 26]. Over time, the GSA was extended to 2D, where a cubic surface was employed to estimate a material's sound behavior [27]. The GSA algorithm has been further adapted by combining multiple curvature operation shapes to make it more sensitive to different defect locations and

by optimizing the order of the smoothing polynomial to improve the accuracy of defect detection [28, 29].

In 2015, the 2D GSA was applied to flash thermographic data, where it enhanced the detectability of defects and reduced the effect of non-uniform heating [24]. Furthermore, it was observed in that study that the size of the spatial gap had a notable effect on the defect detectability. Indeed, the combination of strong non-uniform heating, lateral heat diffusion and measurement noise yields a wide variety of defect signatures. The standard GSA with a fixed spatial gap size has difficulty to cope with these factors in a typical flash IRT dataset.

In this paper, a Multi-Scale Gapped Smoothing Algorithm (MSGSA) is introduced by considering a combination of different spatial gap sizes. This multi-scale implementation significantly improves the detection of different defect sizes in a flash thermographic dataset with typical measurement noise. While this technique is applied here only for flash thermography, it is applicable to all optical infrared thermographic datasets. The structure of the paper is as follows: in section 2, a case study is presented on a synthetic 1D dataset in order to indicate the shortcomings of the standard GSA. Section 3 introduces the procedure of the novel MSGSA, and its effectiveness is demonstrated for the same synthetic 1D dataset. The MSGSA is then extended for 2D datasets, and applied to numerically obtained flash thermography datasets in section 4. Section 5 provides the demonstration of the MSGSA on experimentally obtained flash thermography datasets. Lastly, concluding remarks are gathered in section 6.

2. Gapped Smoothing Algorithm (GSA)

In the original implementation of GSA, a single pixel is considered as the spatial gap and its sound behavior is estimated by fitting a cubic polynomial to its surrounding pixels [25]. However, considering the typical shape of a thermographic amplitude map for a healthy part, a linear polynomial fitting is applied in this paper, which showed to be superior to the cubic polynomial. Additionally, the reduction of the polynomial's order entails a huge reduction in computational effort. Furthermore, a variable spatial gap size is introduced and its effect on defect detectability is studied.

In order to explain the working principles of GSA, a 1D dataset T of n datapoints (i.e. pixels) is assumed in which $T(x_i)$ is the temperature corresponding to the i^{th} pixel, located at x_i . Assuming the linear fitting function and using a gap size of one pixel, any individual pixel x_i is replaced with the mean value of its left and right neighboring pixels x_{i-1} and x_{i+1} . If a bigger (odd valued) gap size of k pixels is used, the central pixel x_i is replaced with the mean value of a group of k neighboring pixels on either side of the spatial gap. This is visually illustrated in **Figure 1(a)** for a spatial gap of $k = 1$ pixels (standard GSA) and in **Figure 1(c)** for $k = 7$ pixels. As such, the gapped smoothed value $\tilde{T}^k(x_i)$ for each pixel x_i corresponding to a spatial gap size k is obtained by the convolution of a kernel matrix M^k (centralized on the evaluation pixel i at location x_i) with the 1D dataset T of length n :

$$\tilde{T}^k(x_i) = \sum_{j=-\frac{3k-1}{2}}^{\frac{3k-1}{2}} M^k[j]T(x_{i+j}) \quad , \quad \text{for } i \in \left[\frac{3k-1}{2} + 1, n - \frac{3k-1}{2} \right] \quad (1)$$

with
$$M^k[j] = \begin{cases} \frac{1}{2k}, & \text{for } j \in [1, k] \vee j \in [2k + 1, 3k] \\ 0, & \text{for } j \in [k + 1, 2k] \end{cases} \quad (2)$$

where \tilde{T} denotes the gapped smoothed value. The kernel matrix M^k is schematically illustrated in **Figure 1(b)** for a gap size $k = 1$ pixel (standard GSA) and in **Figure 1(d)** for $k = 7$ pixels.

Next, the average value of the spatial gap of size k of each pixel x_i , denoted as $\bar{T}^k(x_i)$, is calculated through the convolution of another kernel matrix R^k with the 1D dataset T :

$$\bar{T}^k(x_i) = \sum_{j = -\frac{3k-1}{2}}^{\frac{3k-1}{2}} R^k[j] T(x_{i+j}) \quad , \quad \text{for } i \in \left[\frac{3k-1}{2} + 1, n - \frac{3k-1}{2} \right] \quad (3)$$

with
$$R^k[j] = \begin{cases} 0, & \text{for } j \in [1, k] \vee j \in [2k + 1, 3k] \\ \frac{1}{k}, & \text{for } j \in [k + 1, 2k] \end{cases} \quad (4)$$

where \bar{T} denotes the average value of the spatial gap of size k . The kernel matrix R^k is schematically illustrated in **Figure 1(b)** for a gap size $k = 1$ pixel (standard GSA) and in **Figure 1(d)** for $k = 7$ pixels.

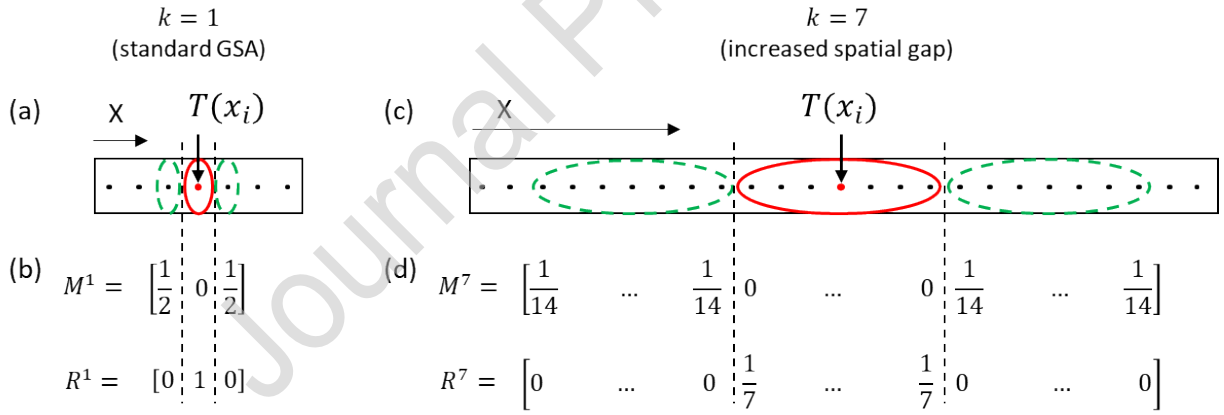


Figure 1: Illustration of the arrangement of pixels used for GSA (top row) and the corresponding kernel matrices M^k and R^k in the case of a spatial gap of (a-b) 1 pixel (standard GSA, $k = 1$); (c-d) 7 pixels ($k = 7$).

Next, the contrast $C^k(x_i)$ between the average of the spatial gap $\bar{T}^k(x_i)$ and the gapped smoothed value $\tilde{T}^k(x_i)$ is calculated:

$$C^k(x_i) = \bar{T}^k(x_i) - \tilde{T}^k(x_i) \quad (5)$$

Then, the dimensionless damage index $DI^k(x_i)$ for a spatial gap of size k is defined as follows [24]:

$$DI^k(x_i) = \frac{(C^k(x_i))^2 \cdot n}{\sum_{i=1}^n (C^k(x_i))^2} \quad (6)$$

where n is the number of pixels in the dataset T and $\sum_{i=1}^n$ the summation over all pixels.

The performance of the standard GSA, i.e. spatial gap size $k = 1$ pixel, is evaluated on a synthetic 1D dataset which is representative for a thermography experiment with various defects. Gaussian-like distributions were used to represent smooth defects (i.e. no abrupt changes). **Figure 2(a)** presents the input to the GSA for the case of perfect data (i.e. no background and noise-free) with defect amplitudes of 0.025, 0.1 and 0.05 for D_1 , D_2 and D_3 respectively. The input signal after adding background non-uniformity is plotted in **Figure 2(c)**. The dominating non-uniform background signal was defined using a Gaussian distribution. Next, white Gaussian noise with a standard deviation of 0.014 was introduced (see **Figure 2(e)**). **Figure 2(b,d,f)** presents the output of the GSA. Application of the GSA on the noise-free datasets yields the damage index values in **Figure 2(b,d)**. D_1 can be detected clearly whereas the other defects have much lower damage index values. Notice that side lobes are obtained for all defects, which are caused by the fact that GSA determines a pixel's damage index by evaluating its surrounding pixels (i.e. smearing effect), as indicated in [25]. Due to the small spatial gap size $k = 1$, the central area of the wide plateau-like defect D_2 remains undetected. Furthermore, after adding noise to the input data (**Figure 2(e)**), the GSA is no longer successful in extracting any of the defects. This is a logical result considering that the used spatial gap only exists of one pixel and is thus almost solely influenced by random noise fluctuations, rather than by the actual defects.

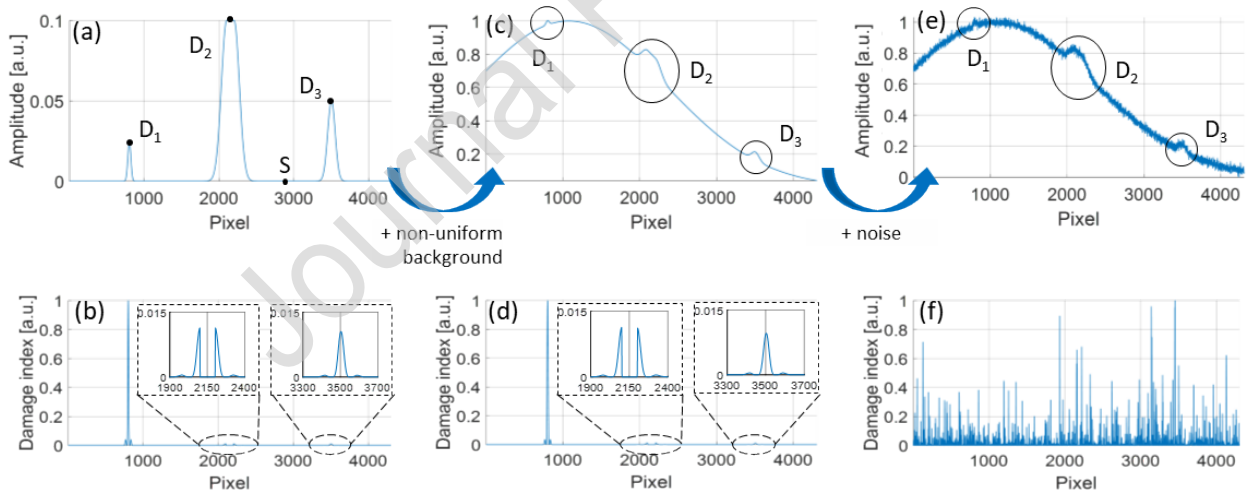


Figure 2: Input to and normalized output from the GSA for: (a-b) perfect data (i.e. no background and noise-free); (c-d) background non-uniformity included; and (e-f) background non-uniformity and noise included.

The results indicate that the spatial gap size of 1 pixel is not effective for the noisy synthetic dataset. Considering that any thermographic experiment contains a comparable level of noise amplitude, it is of interest to investigate whether larger spatial gaps could overcome this limitation.

Thus, the steps in Eq. (1-6) are repeated for all possible (odd valued) spatial gap sizes and at all pixels of the dataset. The resulting damage index value of each pixel in function of the evaluated spatial gap size is visually presented in **Figure 3(a)** for the 1D synthetic input dataset with non-

uniform background and white Gaussian noise (see also **Figure 2(e)**). The regions between the outer pixels and the dashed lines (see **Figure 3(a)**) contain the pixels near the edges for which the corresponding spatial gap sizes are too large to provide a correct damage index value. These regions are thus excluded from the analysis. This figure shows that the evaluated spatial gap size has a significant effect on the damage index value for defects of different sizes. In correspondence with the results shown in **Figure 2(f)**, the presence of white Gaussian noise in the input data strongly affects the defect detectability at small spatial gap sizes, which can be clearly perceived in the bottom rows of **Figure 3(a)**. For a small defect (D_1), the highest damage index is obtained for relatively small spatial gap sizes, whereas a larger defect (D_2) has a higher damage index value for larger spatial gap sizes. The defect with intermediate size (D_3) obviously falls between the defects D_1 and D_2 . The range of useful spatial gap sizes (i.e. with a high damage index value) is much wider for a large defect (D_2) than for a small defect (D_1). However, bigger spatial gap sizes introduce larger side lobes, which means that a sensible upper limit should be imposed on the maximum kernel size. Notice further that for relatively small spatial gap sizes (up to around 75 pixels here), only the edges of the plateau-like defect D_2 are identified, while for larger spatial gap sizes, the plateau of this defect is also visualized. The strong curvature of the synthetic dataset (i.e. background non-uniformity) at the left-hand side causes the damage index in the region around D_1 to slightly increase locally for big spatial gap sizes (**Figure 3(a)**). This is a further motivation to limit the maximum kernel size to a reasonable value. **Figure 3(b)** presents the damage index values as function of the evaluated spatial gap size k for the defects' central pixels (D_1 , D_2 , D_3) and a random sound pixel (S). The damage index value of the sound pixel S shows small random fluctuations for limited spatial gap sizes (up to 51 pixels), after which it remains stable at a near-zero value (**Figure 3(b)**). This figure further supports the observations stated before and suggests an optimal spatial gap size of 37, 171 and 65 pixels for respectively defects D_1 , D_2 and D_3 .

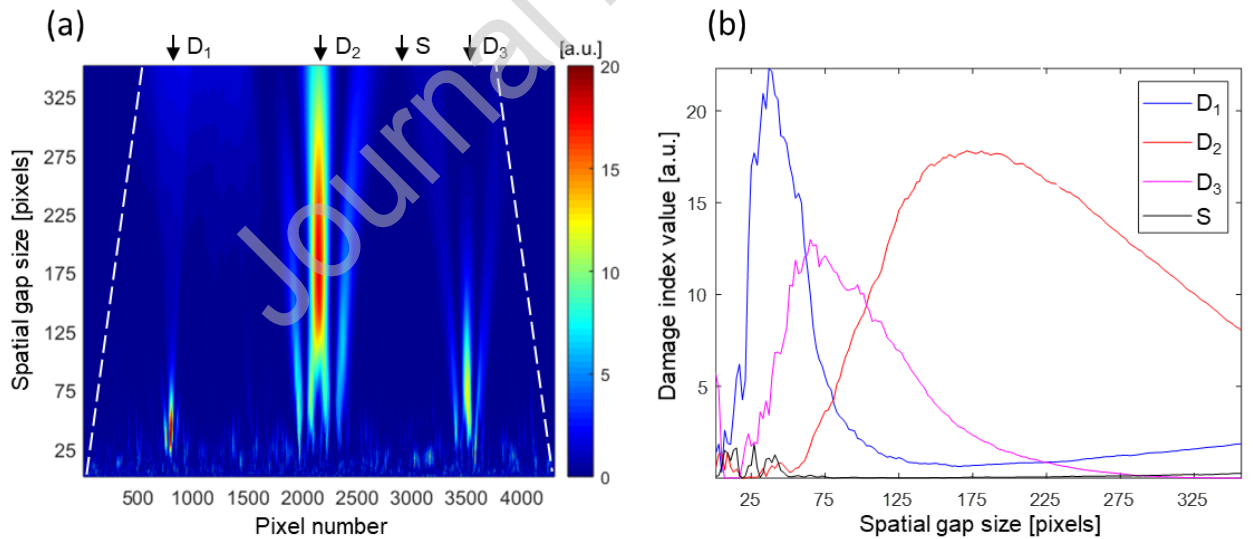


Figure 3: (a) Surface plot of the damage index value in function of the spatial gap size for the 1D synthetic data with background non-uniformity and noise (see **Figure 2(e)**); (b) Damage index in function of spatial gap size for the defects' center pixels and a sound pixel.

Hence, the results suggest that there is an optimal selection of spatial gap size(s) for each defect separately. However, in a typical experimental environment, no prior information about internal defects is available, making this optimal selection of appropriate spatial gap size(s) far from trivial. In order to overcome this complication, a Multi-Scale Gapped Smoothing Algorithm (MSGSA) is introduced in the next section.

3. Multi-Scale Gapped Smoothing Algorithm (MSGSA)

3.1. MSGSA in 1D

The MSGSA processes a 1D dataset through the following series of steps. For the 1D input, the damage index $DI^k(x_i)$ is calculated for each spatial gap size $k = 1, 3, \dots, k_{max}$ and for each pixel x_i through Eq. (1-6). As explained in section 2, a sensible limit should be chosen for the upper bound of the maximum spatial gap size k_{max} . This is expressed in terms of a number of divisions n_d and the number of pixels in the input vector n :

$$k_{max} = 2 \text{ floor}\left(\frac{n}{2n_d}\right) - 1 \quad (7)$$

This definition ensures that the maximum spatial gap size is always an odd value. The number of divisions n_d is set to 12 throughout this paper, which results in a maximum spatial gap size equal to 357 pixels (out of 4303 pixels) in the case of the 1D synthetic dataset. This number was selected such that very large defects are still detectable, while the effect of the non-uniform background is largely suppressed. Thus, the spatial gap sizes k to be evaluated are those ranging from 1 pixel up to 357 pixels, i.e. $k = 1, 3, \dots, 357$.

Considering **Figure 3(a)**, the damage indices obtained from the multiple spatial gap sizes, $DI^k(x_i)$, are combined by application of a combination weighting factor in such a manner that the optimal spatial gap sizes are favored for each pixel x_i . It was observed by the authors that weighting a pixel's damage index value $DI^k(x_i)$ by the mean damage index value of its corresponding spatial gap significantly improved the defect detectability. This guarantees a major contribution of the most effective gap sizes to the global damage index map while a minor contribution of less effective gap sizes to minimize resultant side lobes. By considering the mean value, the effect of random fluctuations is reduced. As such, the combination weight $\alpha^k(x_i)$ of pixel x_i for a spatial gap of size k is determined as:

$$\alpha^k(x_i) = \sum_{j=-\frac{3k-1}{2}}^{\frac{3k-1}{2}} R^k[j] DI^k(x_{i+j}), \quad \text{for } i \in \left[\frac{3k-1}{2} + 1, n - \frac{3k-1}{2}\right], \quad (8)$$

where $k = 1, 3, \dots, k_{max}$

where R^k is the kernel matrix used to calculate averages over a span of size k pixels, centered at pixel x_i (see Eq. (4)). Finally, a global damage index map DI is obtained through the weighted summation of the different damage index maps:

$$DI(x_i) = \sum_k \alpha^k(x_i) \cdot DI^k(x_i), \quad \text{where } k = 1, 3, \dots, k_{max} \quad (9)$$

Applying this set of calculations on the synthetic dataset with non-uniform background and noise (**Figure 4(a)**), i.e. evaluating 179 spatial gap sizes for all 4303 pixels, required 0.1 s to calculate on a laptop with Intel Core i7 CPU and 32 GB of RAM. The output of the MSGSA is plotted in **Figure**

4(b). All three defects are clearly detected, indicating that the proposed algorithm is indeed effective in (i) extracting defects of highly varying sizes, (ii) suppressing noise features and (iii) reducing the background non-uniformity to a near-zero reference level. As a comparison, the output of the standard GSA is also added to **Figure 4(b)** with a thin blue line, clearly indicating the huge improvement of the MSGSA approach. Notice also that the extent of the side lobes is proportional to the size of the defects, which is a consequence of the fact that bigger spatial gap sizes are attributed a larger weighting factor for bigger defects. Furthermore, since the position of the central lobes remains fixed at the defect location while the side lobes extend further away for larger spatial gap sizes (see **Figure 3(a)**), the summation of the damage index maps over all spatial gap sizes (Eq. (9)) causes the MSGSA to suppress the amplitude of the side lobes. The observation that the big defect D_2 has a higher damage index than the other defects can be explained by noting the comparable damage index values for all defects but the larger effective range of spatial gap sizes for D_2 (see **Figure 3(b)**).

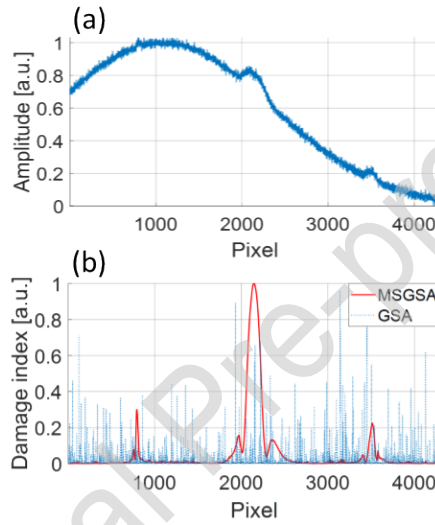


Figure 4: (a) synthetic 1D dataset with background and noise (see **Figure 2(e)**); (b) normalized output from MSGSA and GSA.

3.2. MSGSA in 2D

Considering that thermograms are two-dimensional, the MSGSA should be extended to operate in both X- and Y-direction. Since the above results suggest that rectangular defects should have different optimal spatial gap sizes in X- and Y-direction, the use of a 2D spatial gap (surface fitting procedure) would complicate the optimal detection of rectangular defects significantly. It is opted not to perform a surface fitting procedure because a rectangular spatial gap cannot be fitted properly to all defect shapes (e.g. tilted defects, freeforms, ...), and because such a procedure would significantly increase the calculation times. Instead, the X- and Y-direction of a 2D dataset can be treated separately in the MSGSA. This makes the extension straightforward by applying the MSGSA to each row and each column as if it were multiple 1D input vectors. As such, the row- and column-wise approach of MSGSA can handle all arbitrary defect geometries. The final step of the algorithm for a 2D dataset is to merge the information from both X- and Y-direction into one global damage index map DI :

$$DI(x_i, y_j) = \sqrt{DI_X(x_i, y_j)^2 + DI_Y(x_i, y_j)^2}, \text{ for } i \in [2, n-1] \text{ and } j \in [2, m-1] \quad (10)$$

where n and m are the number of columns and rows, respectively. **Figure 5** provides a graphical overview of the steps of the MSGSA for the two-dimensional case.

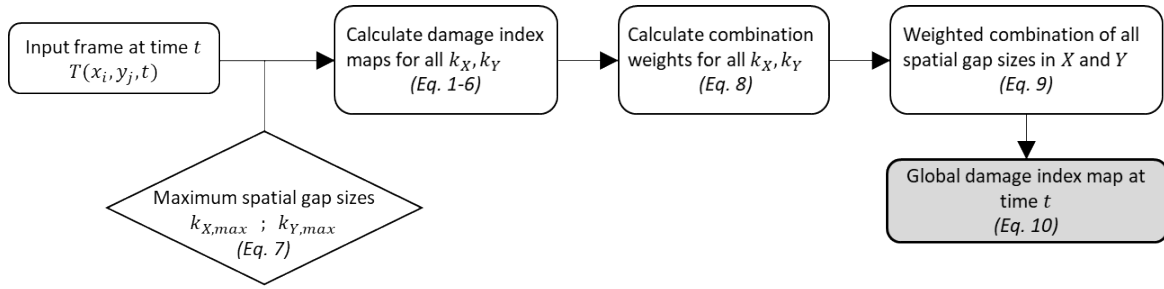


Figure 5: Flowchart of the MSGSA in the 2D case.

4. Numerical verification

In this section, the performance of the MSGSA is evaluated based on a 3D finite element simulation (Abaqus/CAE) of a 2 mm thick CFRP sample. An 8-ply thick CFRP sample with a cross-ply layup of $(0/90)_{2s}$ is modelled using 113,355 brick elements (DC3D20) with quadratic shape functions. Inside the CFRP, eight interply defects are included in between plies 5 and 6 (at a depth of 1.25 mm) through nodal disbonds (i.e. without thermal interactions). As can be seen in the schematic drawing in **Figure 6**, the top three defects are inclined rectangles with varying heights and the bottom three defects are squares of different size. The defects in the middle row are the same as those in the left column, and are added to evaluate the influence of a defect's location in the sample. The tilted defects are specifically selected to illustrate the effectiveness of MSGSA since a 2D spatial gap does not work properly for such defects. The anisotropic thermal diffusivities of a UD lamina (fibers along the X-direction) correspond to $\alpha_X = 1.93 \times 10^{-6} \text{ m}^2/\text{s}$, $\alpha_Y = 4.35 \times 10^{-7} \text{ m}^2/\text{s}$ and $\alpha_Z = 3.78 \times 10^{-7} \text{ m}^2/\text{s}$ [30]. An optical flash lamp with an excitation duration of 5 ms and an energy of 6 kJ is modelled, and located at the right center of the sample (as indicated in **Figure 6**) at an elevation of 250 mm. The lamp's heat flux is modelled by a Gaussian distribution in the XY-plane, providing a non-uniform heating pattern [7]. Thermal interactions with the sample's surroundings through convection and radiation are also considered.

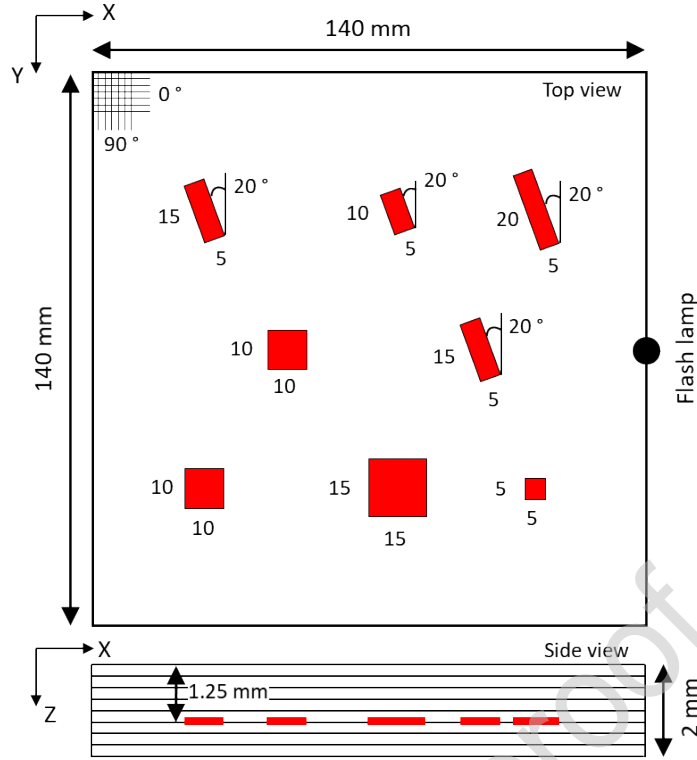


Figure 6: Schematic overview of the modelled CFRP sample (all dimensions are in mm).

The obtained FE solution is mapped to a rectangular grid of 280×280 pixels and is degraded with Gaussian white noise with a temporal standard deviation of 20 mK (equal to the typical NEDT of a high-end IR camera). First, a frame at 0.87 s after the flash excitation is selected (**Figure 7(a)**), in which only some of the defects can be identified due to the strong non-uniform heating and the blurring effect of the 3D heat diffusion. The standard GSA returns only noise and is therefore not added to the discussion. When applying the MSGSA on a 2D dataset, damage index maps in both X- and Y-direction are calculated (Eq. (9)), which are displayed in **Figure 7(b-c)**. All defects can be identified in both damage index maps, and a comparison reveals that both damage index maps are highly similar with comparable damage index values. This indicates that the optimal spatial gap sizes in both directions have been evaluated. Notice that the square defects of $10 \times 10 \text{ mm}^2$ (and also the inclined rectangles of $5 \times 15 \text{ mm}^2$) have different damage index values due to their different locations in the sample. This is explained by considering that the thermal signature of a defect is reduced when it is located further away from the heating source, resulting in a lower thermal contrast and an inferior damage index value. These results indicate that the MSGSA can successfully detect defects of highly different sizes in all directions.

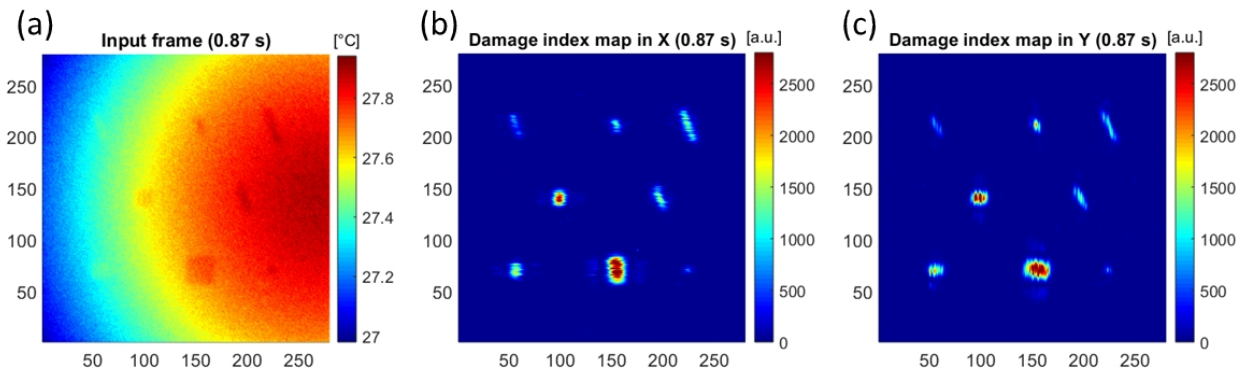


Figure 7: (a) Raw data; (b-c) damage index maps in X- and Y-direction, respectively, at 0.87 s after flash excitation.

Next, three time frames are selected to examine the overall performance of the MSGSA (see **Figure 8**). The frame at 0.63s (**Figure 8(a)**) clearly shows that the flash excitation introduces a significant non-uniform temperature field, with no visual indication of the defects. The output of the standard GSA is purely noise and is therefore not presented. Application of the MSGSA yields a global damage index map which is presented in **Figure 8(b)**. The required calculation time on a standard computer for a frame of this size (280×280 pixels) is on the order of 0.2 s. From this damage index map, 6 of the 8 defects can be identified, however, accurate defect size estimation is not possible due to the significant background noise. The second time frame is at 0.87 s (**Figure 7(a)** and **Figure 8(c)**), in which only some of the defects can be identified due to the strong background non-uniformity and the blurring effect of the 3D heat diffusion. Application of the MSGSA on this second time frame provides the global damage index map as presented in **Figure 8(d)**, in which the extraction of all defects is straightforward and the initially disturbing non-uniformity is now almost completely removed. The markings in **Figure 8(d)** represent the actual locations of the simulated defects, from which it can be observed that the locations and orientations of the defects are preserved by MSGSA. The retrieved defect sizes are slightly smaller than the actual defect sizes. Notice that the sharp corners of the defects are not observed in the global damage index map (nor in the input frame), making the extraction of the exact defect shape difficult. The blurring of such features is a direct consequence of lateral heat diffusion. **Figure 8(e)** presents the third time frame at 1.09 s after flash excitation. The accuracy of defect detection is improved in comparison with the earlier thermograms, however, still not all defects are readily detectable. The output of the MSGSA (**Figure 8(f)**) is also improved (background noise is further reduced), indicating that the quality of the global damage index map increases with the quality of the input frame. As such, there exists a frame of optimal detectability for each defect, which depends on the defect's temperature contrast function. Alternatively, MSGSA could also be applied as an image processing algorithm to the output of other data processing techniques (e.g. PPT, PCT, TSR, ...). This would make the requirement to find and evaluate the frame of optimal detectability (for each pixel) obsolete and would increase the inspectable defect depth range.

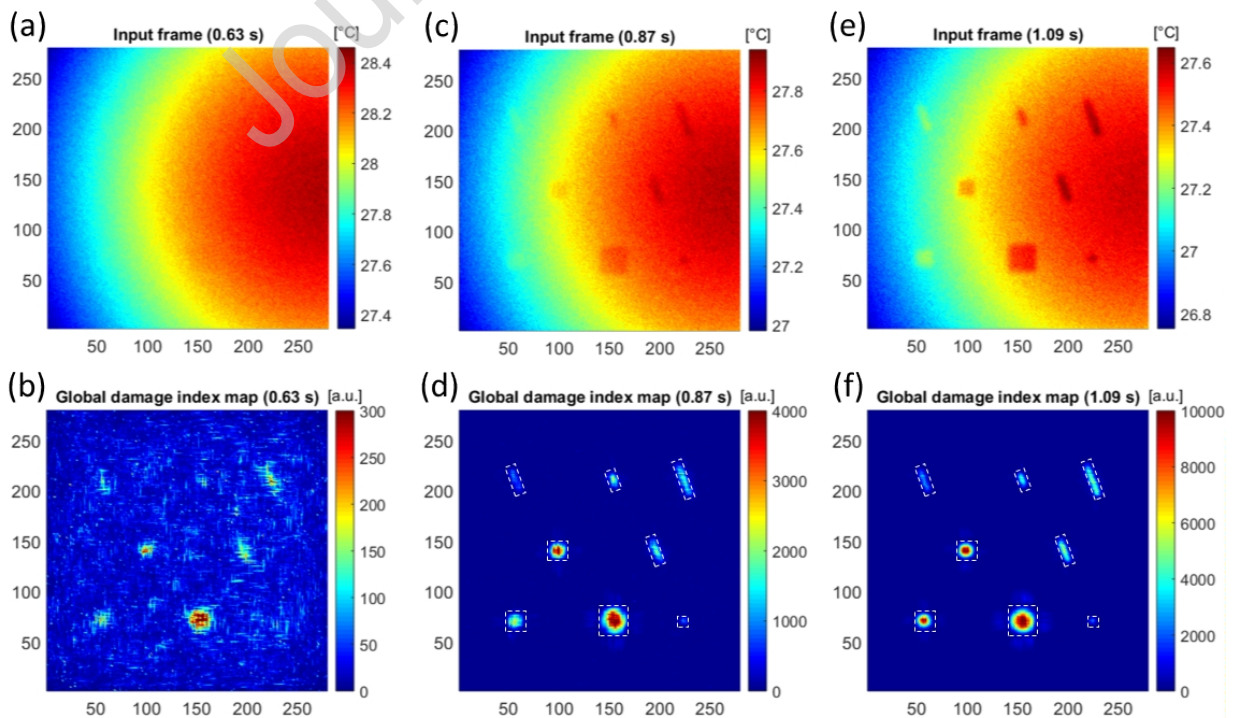


Figure 8: Raw data (top row) and MSGSA output (bottom row) for time frames at (a-b) 0.63 s; (c-d) 0.87 s; (e-f) 1.09 s after flash excitation.

5. Experimental validation

In order to illustrate the effectiveness of the proposed MSGSA experimentally, a 2.9 mm thick CFRP sample with a unidirectional layup of $[0]_{10}$ was investigated through flash thermography. Artificial defects were introduced by placing square, 90 micron thick, ethylene tetrafluorethylene (ETFE) inserts in three rows at different depths, as is schematically illustrated in **Figure 9(a)**. Each row contains a different defect size, and each column has a different defect depth, providing a wide range of size-to-depth ratios.

The sample was optically excited with a Hensel linear flash lamp, which has a flash energy of 6 kJ and a flash duration of around 5 ms. The temperature evolution of the stimulated surface is recorded (i.e. reflection mode) with a FLIR A6750sc. This high-sensitivity infrared (IR) camera has a focal plane array of 640×512 cryo-cooled InSb detectors that have a noise-equivalent differential temperature (NEDT) ≤ 20 mK and is sensitive in the 3-5 μm infrared range. The flash lamp was positioned at ~ 200 mm from the sample, whereas the IR camera was placed ~ 900 mm away. The resultant field of view was 0.5 mm per pixel. The lamp was placed on purpose more on the right side of the sample as to introduce a significant amount of non-uniform heating. A framerate of 25 Hz and an integration time of 531 μs were selected to acquire the thermograms (through Edevis software). A schematic overview of this experimental set-up is provided in **Figure 9(b)**. The recorded sequence was imported into MATLAB in order to perform the MSGSA.

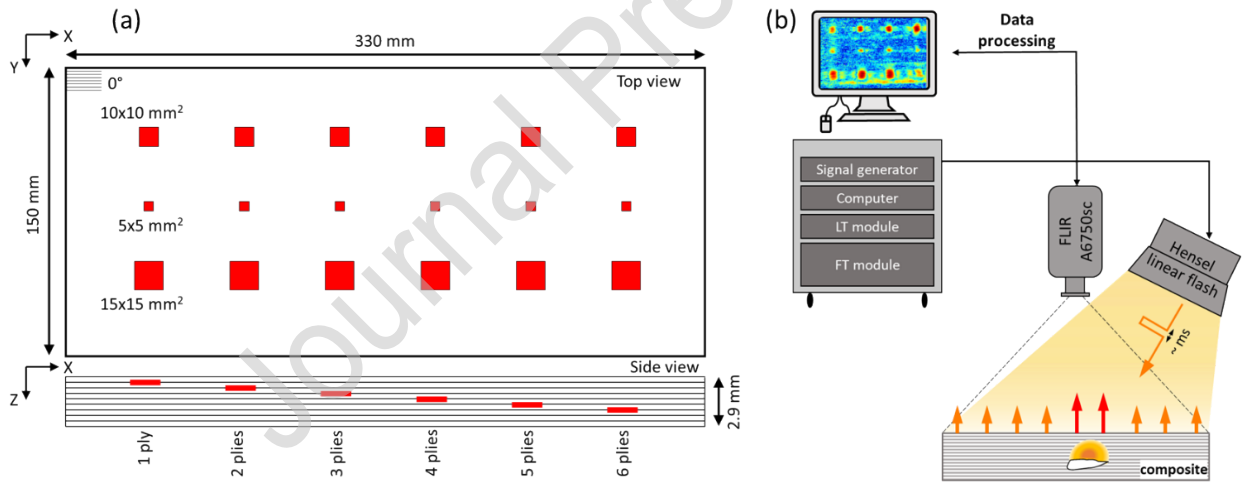


Figure 9: Schematic overview of: (a) the used CFRP sample (1 ply = 0.29 mm); (b) the experimental set-up for flash thermography.

Two thermograms, at 1.52 s and 3 s after the flash excitation, are selected from the complete thermographic sequence. **Figure 10(a)** displays the unprocessed thermographic image at 1.52 s. Considering the known locations of the artificial defects, only the defects at 2 and 3 plies deep are detected. Nonetheless, it is clear that the background non-uniformity would make their detection non-trivial if there would be no prior information about the sample. Because of the relatively early time of this thermogram, the deeper defects are not yet reached by the induced thermal waves and as such do not introduce any thermal disturbance. Also here, the standard GSA was not successful in retrieving any defects and is thus omitted. After application of the MSGSA, a global damage index map (see **Figure 10(b)**) is obtained. The calculation of the MSGSA for this dataset (240×586 pixels) took just under 0.7 s. Whereas the input frame exhibited a

very strong non-uniform background, the MSGSA manages to eliminate this efficiently. In this damage index map, all defects in the three shallowest columns are clearly detected, while the top defect at 4 plies deep is also easily extracted. Furthermore, a localized horizontal disturbance can be perceived just below vertical pixel 50 (at the height of the bottom row of defects). The exact origin of this discontinuity is not clear, however, visual inspection of the sample revealed some imperfections in the surface quality at that location.

Figure 10(c) presents the second thermogram, at 3 s after flash excitation, in which the background non-uniformity is still dominant. A comparison with the input frame at 1.52 s shows that deeper defects have become visible. On the other hand, any indication of the shallow defects has disappeared. The output of the MSGSA (**Figure 10(d)**) successfully removes almost all of the background non-uniformity, and allows for the detection of defects up to the fifth column.

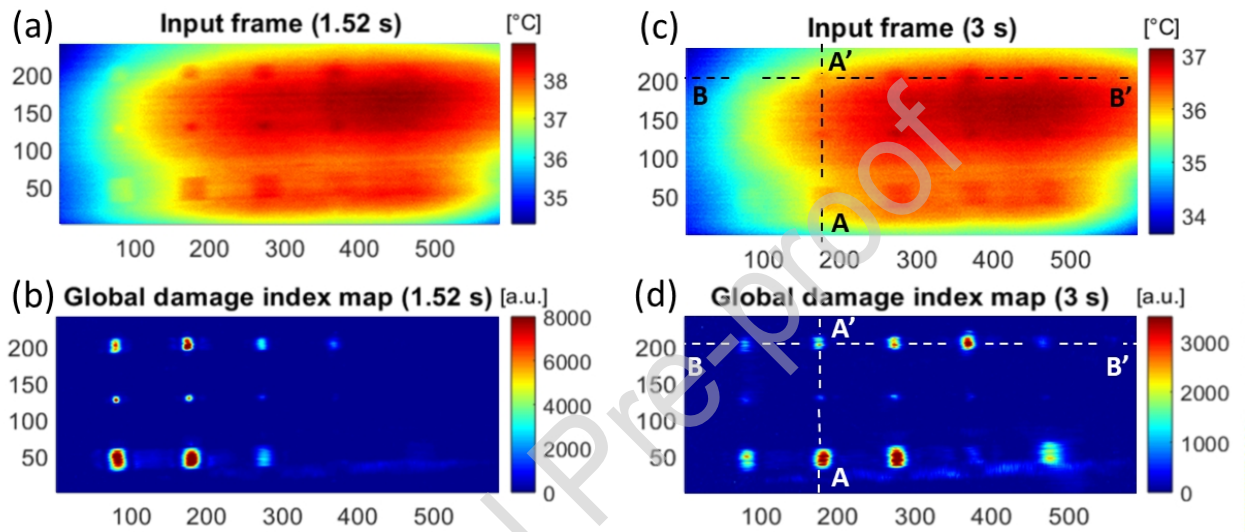


Figure 10: Raw data (top row) and MSGSA output (middle row) for frames at (a-b) 1.52 s and (c-d) 3 s after flash excitation.

Figure 11(a) presents the vertical cross-sectional profile A-A' of the input and output of the MSGSA for the column of defects at 2 plies deep at 3 s after excitation (see **Figure 10(c-d)**). The left vertical axis corresponds to the temperature profile, in which the background non-uniformity is evident, making defect extraction from this temperature data almost impossible. The output of the MSGSA, which is presented on the right vertical axis, clearly indicates all the defects, and also reduces the non-uniformity and noise to a minimum. The horizontal cross-sectional profile B-B' at 3 s is displayed in **Figure 11(b)**. In the temperature profile, the defects at 3 and 4 plies depth can be identified, while all other defects are hidden by the non-uniform background and measurement noise. The profile of the global damage index, on the other hand, provides a very clear identification of the 5 shallowest defects, and even a hint of the deepest one. It is also apparent that the background non-uniformity and the measurement noise are effectively suppressed. Notice that the cross-sectional profiles A-A' and B-B' share a common defect (**Figure 10(c,d)**), however, the global damage index profile A-A' (**Figure 11(a)**) is much less smooth than in section B-B' (**Figure 11(b)**). The leading cause for this observation is the horizontal fiber distribution (along the direction of profile B-B'), providing a smoothing effect in this direction due to the increased lateral heat diffusion along the fibers. The effect of the horizontal fiber distribution can also be observed in the input temperature frames **Figure 10(a,c)**.

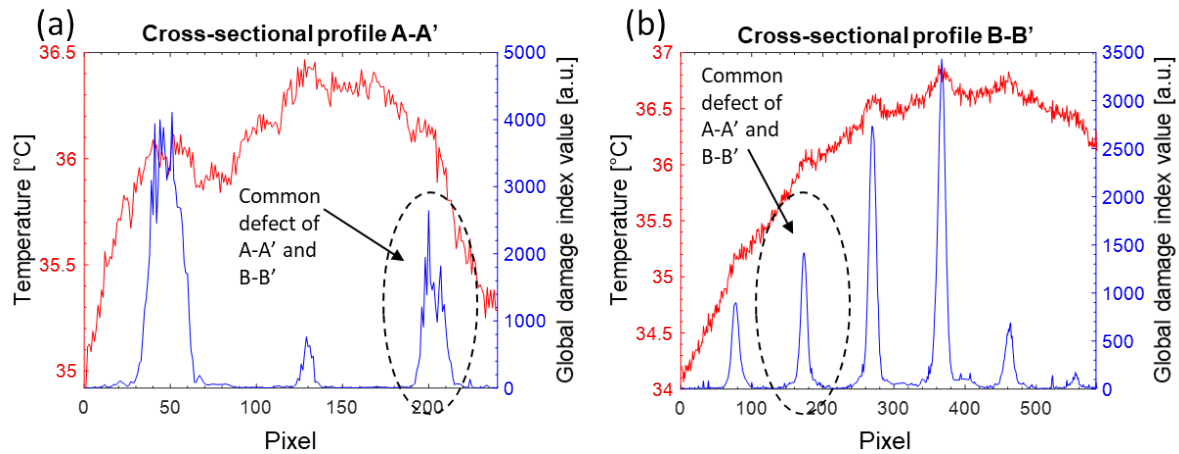


Figure 11: Cross-sectional profiles (bottom row) for the frame at 3 s after flash excitation for (a) A-A' and (b) B-B' (see Figure 10(c-d)).

6. Conclusions

A multi-scale gapped smoothing algorithm (MSGSA) is introduced for the baseline-free processing of noisy thermograms with strong non-uniform background. This MSGSA technique is based on the observation that larger spatial gap sizes are needed to suppress the influence of noise and to detect larger defects. The evaluation of multiple spatial gap sizes and their weighted combination into a single global damage index shows to be effective in detecting all sizes of considered defects. Moreover, it eliminates almost all of the noise and background non-uniformity, and provides a near-zero reference background.

The proposed MSGSA procedure is evaluated on a 1D synthetic dataset including several artificial damage features. Next, its robustness in detection of defects in CFRP samples is demonstrated using both numerical and experimental flash thermographic datasets. The results indicate that the MSGSA is a robust technique, capable of extracting defects of strongly varying sizes, and is effective in suppressing measurement noise and background non-uniformity. Furthermore, the location, orientation and size of the defects after MSGSA correspond well with the input data. Lastly, while the effectiveness of MSGSA has been demonstrated for flash thermography in this contribution, it is in fact also applicable to different heating types.

Acknowledgement

The authors acknowledge the SBO project DETECT-IV (Grant no. 160455), which fits in the SIM research program MacroModelMat (M3) coordinated by Siemens (Siemens Digital Industries Software, Belgium) and funded by SIM (Strategic Initiative Materials in Flanders) and VLAIO (Flemish government agency Flanders Innovation & Entrepreneurship). The authors also acknowledge Fonds voor Wetenschappelijk Onderzoek Vlaanderen (FWO-Vlaanderen) through grants 1S11520N, 1148018N and 12T5418N.

References

1. Yang, R. and Y. He, *Optically and non-optically excited thermography for composites: A review*. Infrared Physics & Technology, 2016. **75**: p. 26-50.
2. Busse, G., D. Wu, et al., *Thermal wave imaging with phase sensitive modulated thermography*. Journal of Applied Physics, 1992. **71**(8): p. 3962-3965.
3. Chatterjee, K., S. Tuli, et al., *A comparison of the pulsed, lock-in and frequency modulated thermography nondestructive evaluation techniques*. NDT & E International, 2011. **44**(7): p. 655-667.
4. Liu, J., W. Yang, et al., *Research on thermal wave processing of lock-in thermography based on analyzing image sequences for NDT*. Infrared Physics & Technology, 2010. **53**(5): p. 348-357.

5. Wang, H., N. Wang, et al., *Phase-locked Restored Pseudo Heat Flux Thermography for Detecting Delamination inside Carbon Fiber Reinforced Composites*. IEEE Transactions on Industrial Informatics, 2018: p. 1-1.
6. Hedayatrasa, S., G. Poelman, et al., *Novel discrete frequency-phase modulated excitation waveform for enhanced depth resolvability of thermal wave radar*. Mechanical Systems and Signal Processing, 2019. **132**: p. 512-522.
7. Hedayatrasa, S., G. Poelman, et al., *Performance of frequency and/or phase modulated excitation waveforms for optical infrared thermography of CFRPs through thermal wave radar: A simulation study*. Composite Structures, 2019. **225**.
8. Laureti, S., G. Silipigni, et al., *Comparative study between linear and non-linear frequency-modulated pulse-compression thermography*. Appl Opt, 2018. **57**(18): p. D32-D39.
9. Tabatabaei, N. and A. Mandelis, *Thermal-wave radar: a novel subsurface imaging modality with extended depth-resolution dynamic range*. Review of Scientific Instruments, 2009. **80**(3): p. 034902.
10. Badghaish, A.A. and D.C. Fleming, *Non-destructive Inspection of Composites Using Step Heating Thermography*. Journal of Composite Materials, 2008. **42**: p. 1337-1357.
11. Almond, D.P., S.L. Angioni, et al., *Long pulse excitation thermographic non-destructive evaluation*. NDT & E International, 2017. **87**: p. 7-14.
12. Wang, Z., G. Tian, et al., *Image processing based quantitative damage evaluation in composites with long pulse thermography*. NDT & E International, 2018. **99**: p. 93-104.
13. He, Z., H. Wang, et al., *Joint Scanning Laser Thermography Defect Detection Method for Carbon Fiber Reinforced Polymer*. IEEE Sensors Journal, 2020. **20**(1): p. 328-336.
14. Milne, J.M. and W.N. Reynolds, *The non-destructive evaluation of composites and other materials by thermal pulse video thermography*. Thermosense VII, 1985: p. 119-1222.
15. Ibarra-Castanedo, C., D.A. González, et al., *On signal transforms applied to pulsed thermography*. Recent Res. Devel. Applied Phys., 2006. **9**.
16. Maldague, X. and S. Marinetti, *Pulse phase infrared thermography*. Journal of Applied Physics, 1996. **79**(5): p. 2694-2698.
17. Oswald-Tranta, B., *Time and frequency behaviour in TSR and PPT evaluation for flash thermography*. Quantitative InfraRed Thermography Journal, 2017. **14**(2): p. 164-184.
18. Rajic, N. and DSTO-TR-1298, *Principal Component Thermography*. 2002, Defence Science and Technology Organisation Victoria (Australia) Aeronautical and Maritime Research Lab. p. 38.
19. Shepard, S.M., *Temporal noise reduction, compression and analysis of thermographic data sequences*. 2003, Thermal Wave Imaging, Inc.: US.
20. Vavilov, V.P. *Dynamic Thermal Tomography: New NDE Technique to Reconstruct Inner Solids Structure Using Multiple IR Image Processing*. in *Review of Progress in Quantitative Nondestructive Evaluation*. 1992.
21. Vavilov, V.P., *Dynamic thermal tomography: Recent improvements and applications*. NDT & E International, 2015. **71**: p. 23-32.
22. Ciampa, F., P. Mahmoodi, et al., *Recent Advances in Active Infrared Thermography for Non-Destructive Testing of Aerospace Components*. Sensors (Basel), 2018. **18**(2).
23. Ibarra-Castanedo, C., D. González, et al., *Infrared image processing and data analysis*. Infrared Physics & Technology, 2004. **46**(1-2): p. 75-83.
24. Li, B., L. Ye, et al., *Gapped smoothing algorithm applied to defect identification using pulsed thermography*. Nondestructive Testing and Evaluation, 2015. **30**(2): p. 171-195.
25. Ratcliffe, C.P., *Damage detection using a modified Laplacian operator on mode shape data*. Journal of Sound and Vibration, 1997. **204**(3): p. 505-517.
26. Ratcliffe, C.P. and W.J. Bagaria, *Vibration Technique for Locating Delamination in a Composite Beam*. AIAA Journal, 1998. **36**(6): p. 1074-1077.
27. Wu, D. and S.S. Law, *Damage localization in plate structures from uniform load surface curvature*. Journal of Sound and Vibration, 2004. **276**(1-2): p. 227-244.
28. Rucevskis, S., R. Janeliukstis, et al., *Mode shape-based damage detection in plate structure without baseline data*. Structural Control and Health Monitoring, 2016. **23**(9): p. 1180-1193.
29. Cao, S. and H. Ouyang, *Output-Only Damage Identification Using Enhanced Structural Characteristic Deflection Shapes and Adaptive Gapped Smoothing Method*. Journal of Vibration and Acoustics, 2017. **140**(1).
30. Maierhofer, C., M. Röllig, et al., *Evaluation of Different Techniques of Active Thermography for Quantification of Artificial Defects in Fiber-Reinforced Composites Using Thermal and Phase Contrast Data Analysis*. International Journal of Thermophysics, 2018. **39**(5).

24 February 2020

Dear Editor-in-Chief of Journal of NDT&E International,

This is to certify that all authors of the manuscript “*Multi-Scale Gapped Smoothing Algorithm for Robust Baseline-free Damage Detection in Optical Infrared Thermography*”, by Gaétan Poelman, Saeid Hedayatrasa, Joost Segers, Wim Van Paepegem and Mathias Kersemans, have agreed with its publication by NDT&E International and have no conflict of interest in the subject matter or materials discussed in this manuscript.

With best regards,

Gaétan POELMAN



FACULTY OF ENGINEERING
AND ARCHITECTURE

ir. Gaétan Poelman

Doctoral student – NDT of composites by thermography

FWO Aspirant Strategic Basic Research

T +32 (0)9 331 04 34

Mechanics of Materials and Structures

Department of Materials, Textiles and Chemical Engineering

Technologiepark 46, B-9052 Zwijnaarde (Gent), Belgium

Declaration of interests

☒ The authors declare that they have no known competing financial interests or personal relationships that could have appeared to influence the work reported in this paper.

☐ The authors declare the following financial interests/personal relationships which may be considered as potential competing interests:

--